THE IMPACT OF GAS BULK ROTATION ON THE LYMAN-α LINE

Juan N. Garavito-Camargo[1], Jaime E. Forero-Romero[1], Mark Dijkstra[2]
Submitted for publication in ApJ

ABSTRACT

We present results of radiative transfer calculations to measure the impact of gas bulk rotation on the morphology of the Lyman α emission line in distant galaxies. We model a galaxy as a sphere with a homogeneous mixture of dust and hydrogen at a constant temperature. These spheres have a solid-body rotation with maximum velocities in the range $0 - 300$ km s^{-1} and neutral hydrogen optical depths in the range $\tau_{\rm H} = 10^5 - 10^7$. We also consider two kinds of spatial distribution for the radiation sources with respect to the sphere: central and homogeneous. Our main finding is that the line width and the intensity at the line's center increase with rotational velocity. For homogeneously distributed sources the line becomes single peaked at rotational velocities larger than the line width in the static case. Under the same conditions the escape fraction increases $\sim 30\%$. For radiation sources located off-center, the line morphology presents a range of single, double and triple peaks. We show how these results are useful to interpret recent spectroscopic results of distant $z \sim 2 - 3$ star forming galaxies.

Subject headings: galaxies: high-redshift, galaxies: star formation, line: formation

1. INTRODUCTION

The detection of strong Lyα emission lines has become an essential method in extra-galactic astronomy to find distant star-forming galaxies (Partridge & Peebles 1967; Rhoads et al. 2000; Gawiser et al. 2007; Koehler et al. 2007; Ouchi et al. 2008; Yamada et al. 2012; Schenker et al. 2012). The galaxies detected using this method receive the name of Lyα emitters (LAEs). A detailed examination of this galaxy population has diverse implications for galaxy formation, reionization and the large scale structure of the Universe. Attempts to fully exploit the physical information included in the Lyα line require an understanding of all the physical factors involved in shaping the line. Due to the resonant nature of this line, these physical factors notably include temperature, density and bulk velocity field of the neutral Hydrogen in the emitting galaxy and its surroundings.

A basic understanding of the quantitative behavior of the Lyα line has been reached through analytic studies in the case of a static configurations, such as uniform slabs (Harrington 1973; Neufeld 1990) and uniform spheres (Dijkstra et al. 2006). Analytic studies of configurations including some kind of bulk flow only include the case of a sphere with a Hubble like expansion flow (Loeb & Rybicki 1999).

A quantitative description of the Lyα line has been reached through Monte Carlo simulations (Auer 1968; Avery & House 1968; Adams 1972). In the last two decades these studies have become popular due to the availability of computing power. Early into the 21st century, the first studies focused on homogeneous and static media (Ahn et al. 2000, 2001; Zheng & Miralda-Escudé 2002); Later on, the effects of clumpy media (Hansen & Oh 2006) and expanding/contracting shell/spherical geometries started to be studied (Verhamme et al. 2006;

Dijkstra et al. 2006). Similar codes have applied these results to semi-analytic models of galaxy formation (Orsi et al. 2012) and results of large hydrodynamic simulations (Forero-Romero et al. 2011, 2012; Behrens & Niemeyer 2013). Recently, Monte Carlo codes have also been applied to the results of high resolution hydrodynamic simulations of individual galaxies(Laursen et al. 2009; Barnes et al. 2011; Verhamme et al. 2012; Yajima et al. 2012). Meanwhile, recent developments have been focused on the systematic study of clumpy outflows (Dijkstra & Kramer 2012)and anisotropic velocity configurations (Zheng & Wallace 2013).

The recent studies of galaxies in hydrodynamic simulations (Laursen et al. 2009; Barnes et al. 2011; Verhamme et al. 2012; Yajima et al. 2012) have all shown systematic variations in the Lyα line with the viewing angle. These variations are a complex superposition of anisotropic density configurations (i.e. edge-on vs. face-on view of a galaxy), the inflows observed by gas cooling and the outflows included in the supernova feedback process of the simulation. These bulk flows physically correspond to the circumgalactic and intergalactic medium (CGM and IGM). These effects are starting to be studied in simplified configurations that vary the density and wind characteristics (Zheng & Wallace 2013).

However, in all these efforts the effect of rotation, which is an ubiquitous feature in galaxies, has not been systematically studied. The processing of the Lyα photons in a rotating interstellar medium (ISM) must have some kind of impact in the Lyα line morphology.

Performing that study is the main goal of this paper. We investigate for the first time the impact of rotation on the morphology of the Lyα line. We focus on a simplified system: a spherical gas cloud with homogeneous density and solid body rotation, to study the line morphology and the escape fraction in the presence of dust. We base our work on two independent Monte Carlo based radiative transfer codes CLARA (Forero-Romero et al. 2011) and XX (Dijkstra & Kramer 2012) .

[1] Departamento de Física, Universidad de los Andes, Cra. 1 No. 18A-10, Edificio Ip, Bogotá, Colombia
[2] Max Planck Institute for Astrophysics, Karl-Schwarzschild-Str. 1, 85741, Garching, Germany

This paper is structured as follows: In §2 we present the implementation of bulk rotation into the Monte Carlo codes, paying special attention to coordinate definitions. We also present a short review of how the Lyα radiative transfer codes work and list the different physical parameters in the simulated grid of models. In the next §3 we present the results of the simulations, with special detail to quantities in the line that show a clear evolution as a function of the sphere rotational velocity. In §4 we discuss the implications of our results in the interpretation of LAEs observations. In the last section we present our conclusions.

In this paper we express a photon's frequency in terms of the dimensionless variable $x \equiv (\nu - \nu_a)/\Delta\nu_\alpha$, where $\nu_\alpha = 2.46 \times 10^{15}$ Hz is the Lyα resonance frequency, $\Delta\nu_\alpha \equiv \nu_\alpha\sqrt{2kT/m_pc^2} \equiv \nu_a v_{\text{th}}/c$ is the Doppler broadening of the line which depends on the neutral gas temperature T scattering the radiation or equivalently the thermal velocity v_{th} of the atoms. For the temperature $T = 10^4$K used in our radiative transfer calculations the thermal velocity is $v_{th} = 12.8\,\text{km s}^{-1}$.

2. MODELS OF BULK GAS ROTATION

Describing the kinematics of gas rotation in all generality is a complex task, specially at high redshift where there is still missing a thorough observational account of rotation in galaxies beyond $z > 1.0$. Event at low red-shifts there is a great variation in the shape of the rotation curve as observed in HI emission as a function of the distance to the galaxy center. However there are two recurrent features. First, in the central galactic region the velocity increases proportional to the radius, following a solid rotation behavior. Second, beyond a certain radius the rotation curve tends to flatten.

An ab-initio description of realistic rotation curves in simulations depends on having access to the dynamic evolution of all mass components in the galaxy: stars, gas and dark matter. Such level of realism is extremely complex to achieve, specially if one wants to get a systematic description based on statistics of simulated objects.

Following the tradition of studies of Lyα emitting systems, we implement a model with simplified geometry. We assume that the gas is homogeneously distributed in a sphere that rotates as a solid body with constant angular velocity. This simple model will contain only one free parameter: the linear velocity at the sphere's surface, V_{max}.

2.1. Detailed Implementation of Rotation

In the Monte Carlo code we define a Cartesian coordinate system to describe the position of each photon. The origin of this system coincides with the center of the sphere and the rotation axis is defined to be z-axis. With this choice, the components of the gas bulk velocity field, $\vec{v} = v_x\hat{i} + v_y\hat{j} + v_z\hat{k}$, can be written as

$$v_x = -\frac{y}{R}V_{\text{max}}, \tag{1}$$

$$v_y = \frac{x}{R}V_{\text{max}}, \tag{2}$$

$$v_z = 0, \tag{3}$$

where R is the radius of the sphere and V_{max} is the linear velocity at the sphere's surface. The minus/plus sign in

the x/y-component of the velocity indicates the direction of rotation. In this case we take the angular velocity in the same direction as the $\hat{k}$ unit vector. With these definitions we can write the angular velocity as $\omega = V_{\text{max}}/R$.

For each photon in the simulation we have its initial position inside the sphere, direction of propagation $\hat{k}_{in}$ and reduced frequency x_{in}. The photon's propagation stops once they cross the surface of the sphere. At this point we store the position, the outgoing direction of propagation $\hat{k}_{out}$ and the reduced frequency x_{out}. We define the angle Θ by $\cos\Theta = \hat{k} \cdot \hat{k}_{out}$, that is the polar angle of the outgoing photon with respect to the z axis. Following Zheng & Wallace (2013) we make the study of the anisotropic emission in terms of this angle..

2.2. Brief Description of the Radiative Transfer Codes

Here we briefly describe the relevant points for the two radiative transfer codes we have used. For a detailed description we refer the reader to the original papers Forero-Romero et al. (2011); Dijkstra & Kramer (2012).

The codes follow the individual scatterings of Lyα photons as it travels through a 3D distribution of neutral Hydrogen. At each scattering the frequency of the photon (in the laboratory frame) and its direction of propagation change. This change in frequency is due to the peculiar velocities of the Hydrogen atom that absorbed and reemitted the photon. If dust is present, the photon can interact either with a Hydrogen atom or dust grain. In the case of a dust interaction the photon can be either absorbed or scattered, this probability is encoded in the dust albedo, A, which we chose to be $1/2$. In order to obtain accurate values for the escape fraction of photons in the presence of dust, we do not use any accelerating mechanism in the radiative transfer. Once the photons escape the gas distribution we store their direction at their direction of propagation and frequency at their last scattering.

The photons are thus emitted in some region of the gas distribution and follow a random walk in space and frequency until they escape the gas distribution or are absorbed by a dust grain. The initialization process for the Lyα photons has to specify its position, frequency and direction of propagation. In our case we select the initial frequency to be exactly the Lyα restframe frequency ($x = 0$) and the direction of propagation to be random following an flat probability distribution over the sphere.

The gas is completely defined by its geometry (i.e. sphere or slab), temperature T, Hydrogen optical depth τ_{H}, dust optical depth τ_{a} and the bulk velocity field $\vec{v}$. Here we treat the gas as homogeneous in density (τ_{H}, τ_{a}) and temperature.

2.3. Grid of Simulated Galaxies

In the Monte Carlo calculations we follow the propagation of $N_\gamma = 10^5$ numerical photons through different spherical galaxies. For each galaxy we vary at least one of the following parameters: the maximum rotational velocity V_{max}, the hydrogen optical depth τ_H, the dust optical depth τ_a and the initial distribution of photons with respect to the gas. There are 60 models initial combining all variations of the input parameters. Table 1 summarizes the models.
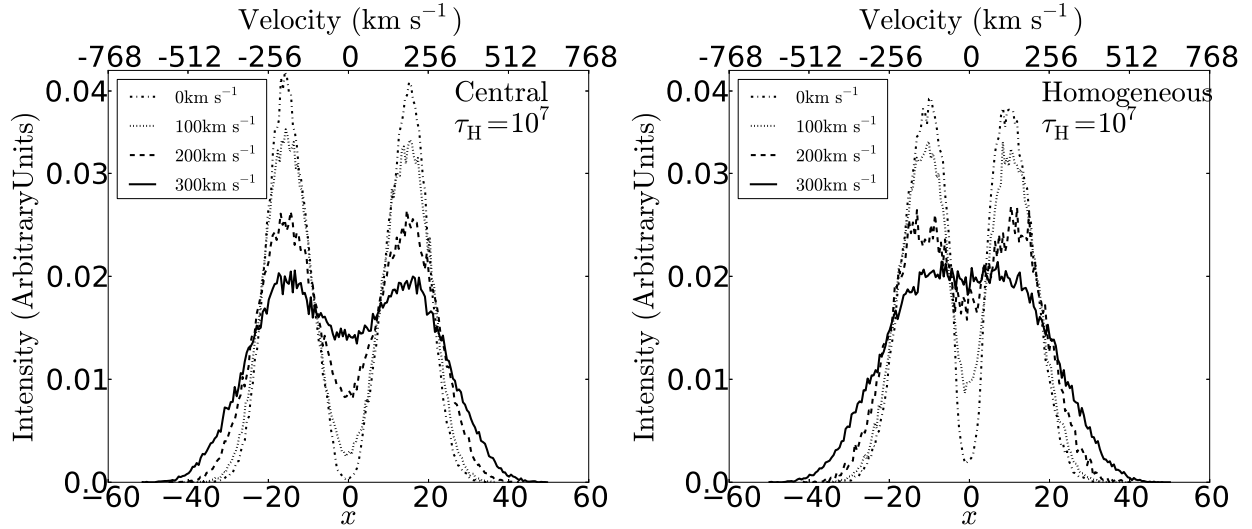
FIG. 1.— Shape of the Lyα line for different velocities rotational velocities for spherical distributions with $\tau_H = 10^7$. The left (right) panel shows the central (homogeneous) photon distribution. All photons were taken into account regardless of their final direction of propagation.

Physical Parameter (units)	Symbol	Values
Velocity (km s^{-1})	V_{max}	0, 50, 100, 200, 300
Hydrogen Optical Depth	τ_H	10^5, 10^6, 10^7
Dust Optical Depth	τ_a	0,1
Photons Distributions		Central, Homogeneous

TABLE 1
LIST OF THE PHYSICAL PARAMETERS THAT DEFINE THE SPHERICAL MODELS SIMULATED IN OUR MONTE CARLO CALCULATIONS. FOR EACH PARAMETER WE VARY THE VALUES IN THE RANGE LISTED IN THE LAST COLUMN. TAKING INTO ACCOUNT ALL THE POSSIBLE COMBINATIONS WE END UP WITH 60 DIFFERENT MODELS.

Additionally, we have used two independently developed Monte Carlo codes (Forero-Romero et al. 2011; Dijkstra & Kramer 2012) to perform the calculations of the non-dusty models. The results we report are robust in the sense that they are obtained by both codes.

3. RESULTS

The central result of this paper is summarized in Figure 1. It shows the evident impact of rotation on the morphology of the emergent Lyα line. Both panels focus on the results for $\tau_H = 10^7$, showing that the influence of rotation is present both when the photons are either homogeneously or centrally initialized over the gas volume.

In the next subsections we characterize the line morphology by the half-width at half intensity and the peak maxima. In order to interpret the morphological changes in the line we also report the median number of scatter for each Lyα photon in the simulation. For the models where dust is included we measure the escape fraction as a function of rotational velocity. Finally, we make an estimate of the anisotriopic emission of the models in comparison with static spheres.

3.1. Line width and peak maxima

There are three clear effects on the line's morphology as the rotational veloctiy increases. First, the line broadens; second, the double peaks reduce their intensity; and
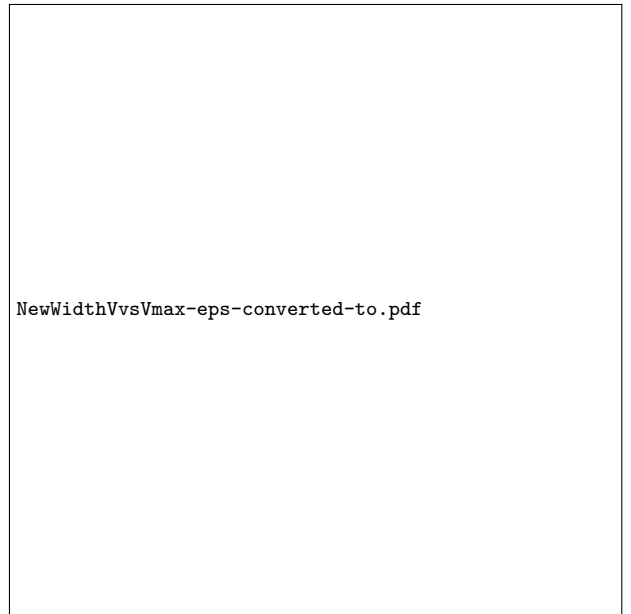

FIG. 2.— Half-width for the non-dusty models as a function of rotational velocity V_{max}. Continuous (dashed) lines correspond to central (homogeneous) source distributions.

third, the intensity at the line center rises. The two last effects give the impresion that the double peaks are merger into one at high rotational velocities, a result that is evident for the homogeneously distributed sources as shown in right panel in Figure 1.

We use the full width at half maximum (FWHM), W, to quantify the line broadening. Figure 2 shows how W increases with rotational velocity. **Here we need to check the numbers to say something more specific.**

We parameterize the dependency of the linewidth as $W^2 = W_0^2 + V_{max}^2/\lambda^2$, where W_0 is the velocity width in the static case and λ is a positive scalar to be determined as a fit to the data. With this test we want to know to what extent the new velocity witdth can be expressed
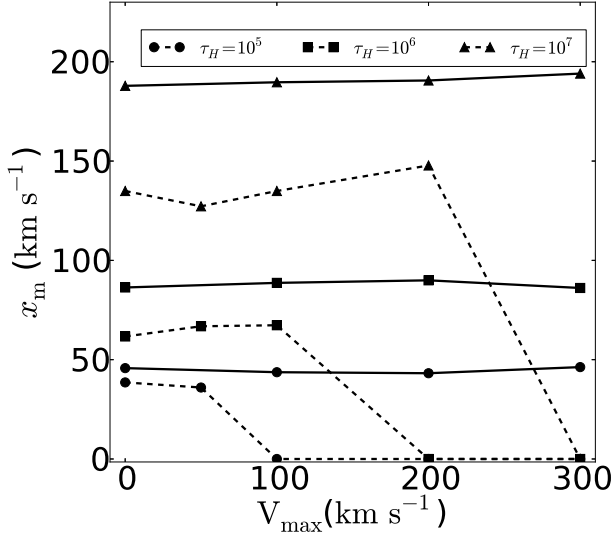
FIG. 3.— Position of the peak maxima as a function of rotational velocity V_{max}. Continuous (dashed) lines correspond to central (homogeneous) source distributions. A value of $x_{max} = 0$ indicates that line becomes single peaked.
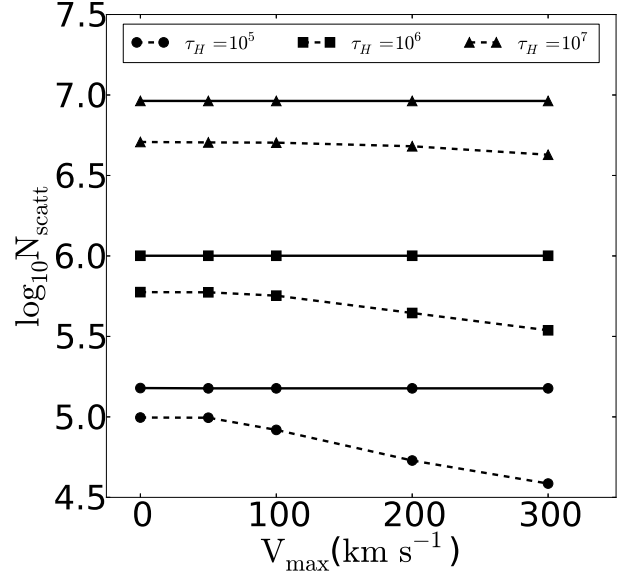

FIG. 4.— Logarithm of the average number of scatterings as function of rotational velocity. Continuous (dashed) lines represent an central (homogeneous) distribution of sources.

as a quadratic sum of the two relevant velocities in the problem. We find that for $\lambda = x \pm y$ ($\lambda = x \pm y$) for the central (homogeneous) sources.

In order to quantify the transition to a single peak we measure the position for the peak maxima as a function of the rotational velocity. Our results are presented in Figure 3 where it is clear that for central sources there are always two peaks with fixed positions as the rotational velocity changes. However, in the case of homogeneously emitted sources the maxima position remain close to constant until some velocity threshold the line becomes single peaked with $x_m = 0$ km s^{-1}. **By inspection we find that in all cases the transition has occurred when the rotational velocity is larger than the intrinsic linewidth OR HALF WIDTH ONCE THE NUMBERS ARE FIXED?**.

One possible explanation for the emergence of the single peak in the homogeneous source systems is that some photons close to the surface (a sort of photosphere) can escape with a low number of scatterings, allowing them to stay close to the line's center. Increasing the rotational velocity V_{max} reduces the optical depth making the photosphere region effectively larger, increasing the number of photons escaping close to the line's center.

However, for the central emission the transition to a single peak is never completed in the range of explored parameters. The absence of a single peak phase could be partially explained by the absence of a photosphere, in this case the average number of scatterings to escape should remain close to constant as the rotational velocity increases. The rise in intensity at the line's center could instead mean that the scattering in a medium with bulk motion are inefficient in driving photons outside that frequency region.

In order to explore our interpretation for these two scenarios we now quantify the effect of rotation on the number of scatterings.

3.2. *Average Number of Scatterings*

The number of scatterings affects the escape frequency of a Lyα photon. In static cases, a large value of the optical depth correlates with a high number of scatterings, increasing the probability of finding a Lyα photon far from the line's center. As a result the peak maxima shifts from the center as the amount of neutral hydrogen increases. This can be precisely quantifyied in the static slab with central sources where the maxima position are related to the optical depth and the temperature as $x_m = \pm 1.066(a\tau_H)^{1/3}$ (Harrington 1973). In the same model the average number of scatterings depends only on the optical depth $\langle N_{scatt} \rangle = 1.612\tau_H$ (Adams 1972; Harrington 1973), in the case of homogeneously distributed sources $\langle N_{scatt} \rangle = 1.16\tau_H$ (Harrington 1973).

In Figure 4 we show the average number of scatterings $\langle N_{scatt} \rangle$ as a function of the rotational velocity V_{max}. For the central source distribution the average number of scatterings $\langle N_{scatt} \rangle$ changes less than 0.5% for different velocities. In this setup the number of scatterings is proportional to the optical depth, with $\langle N_{scatt} \rangle = (1.50, 1.00, 0.92)\tau_H$ for optical depth values of $\tau_H = (10^5, 10^6, 10^7)$, respectively

From Figure 4 is also clear that for the homogeneous distribution there is a clear decrease of $\langle N_{scatt} \rangle$ as the V_{max} increases. For instance, for $\tau_H = 10^5$ the average number of scatterings decreases by 61% at $V_{max} = 300$ km s^{-1} in comparison to the static case.

In this case we find that for a static sphere $\langle N_{scatt} \rangle = (0.99, 0.59, 0.51)\tau_H$, this representsfactors of $(0.66, 0.59, 0.55)$ lower than the centrally emitted photons. In contrast the analytic solution for the homogeneous slab gives 0.72 times less scatterings in the homogeneous case than in the central one.

In order to gain a deeper understanding of these results and explain the results for the maxima in the line morphology we make 2D histograms for the number of scatterings as a function of the outgoing dimensionless frequency x. In Figure 5 we show such histogram in the case $\tau_H = 10^5$ for the static case and $V_{max} = 300$ km s^{-1}.
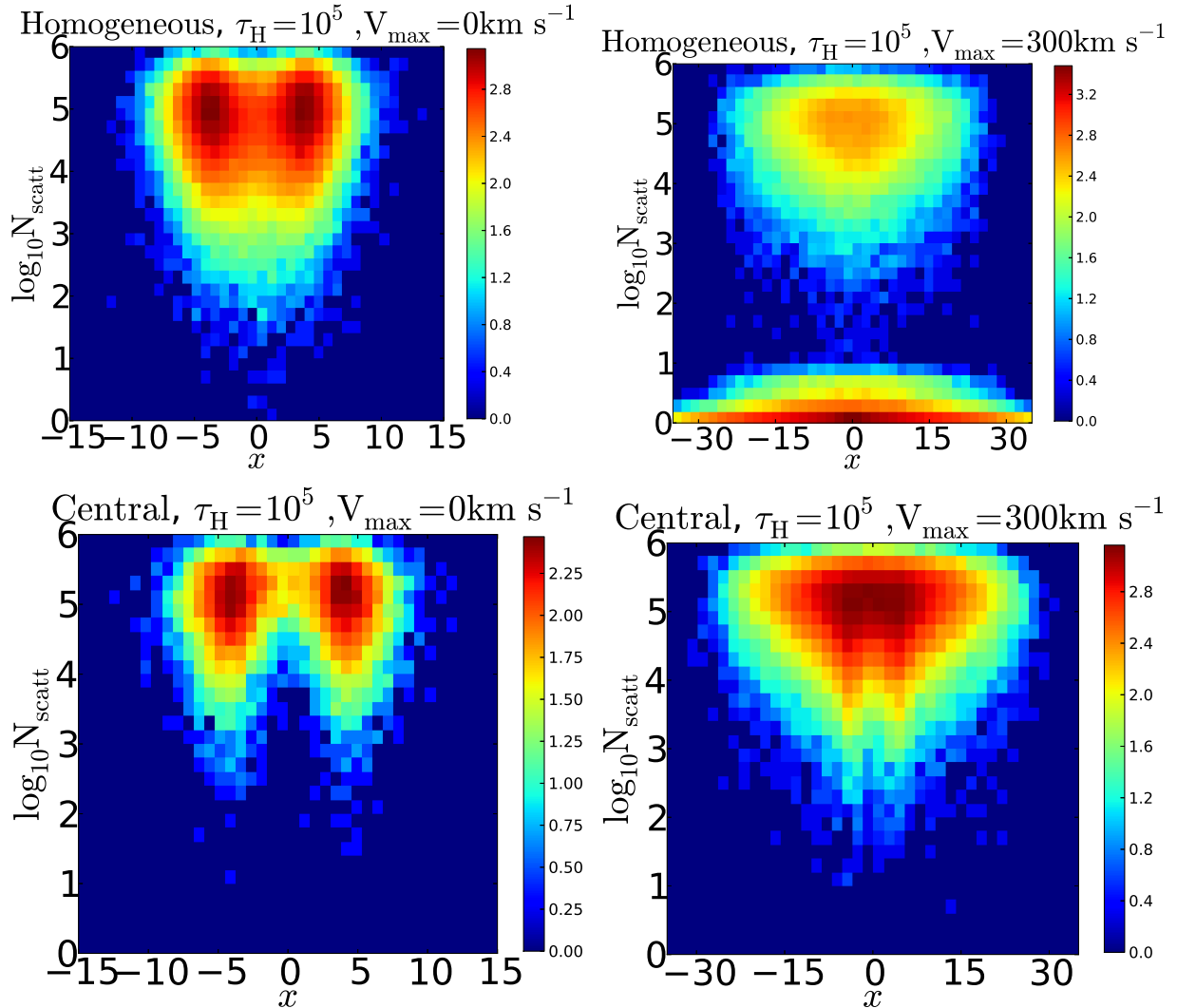
FIG. 5.— 2D histogram of $N_{\rm scatt}$ vs x. The upper (lower) panels show the homogeneous (central) source distribution. Left corresponds to the static case and right $V_{\rm max} = 300\,{\rm km\,s^{-1}}$. The color scale is logarithmic on the number of photons with given values of $N_{\rm scatt}$ and x.

The upper (lower) panels show the results for the homogeneous (central) source distribution. The color scale is logarithmic in the number of photons at a certain value x-$N_{\rm scatt}$.

The top right panel of Figure 5 (homogeneous sources, high rotational velocity) supports our hypothesis about the photo-sphere in the homogeneous distribution. In this case most of the photons that left with $x \sim 0$ have escaped with less than 10 scatterings. This also explains the decrease in the average number of scatterings observed in Figure 4.

However, for a central distribution the situation is quite different (lower panels). In this case the number of scatterings remains high, in the order of the optical depth, but the two peaks do get closer to each other. Here the most probable physical picture is that each scattering, due to the bulk velocity of the gas, is inefficient in driving the photon outside the line center.

3.3. Dusty Clouds: Escape Fraction

In the case of dusty clouds, all changes in the average number of scatterings presented in the previous subsection have a direct bearing on the escape fraction. From the results we have just obtained we can predict that for central source distributions the escape fraction will barely change, while larger effects should be expecte for homogeneously distributed sources.

Figure 6 confirm these expectations. It shows the escape fraction as a function of the rotational velocity. The curves for the central source distribution stay flat, while for the homogeneous case there is a clear rise with rotational velocity. Rotation has a higher relative impact in the models with low optical depth. For instance, in models with $\tau_{\rm H} = 10^5$, the static scape fraction is 0.26 and increases to 0.37 for $V_{\rm max} = 300$ km s^{-1}. Table **??** lists all the values for the escape fraction **We also need a table listing the escape fraction values.**

In Figure 7 we put these results in the context of the analytic solution for the infinite slab (Neufeld 1990). In Neufeld's set-up the analytic solution depends uniquely on the product $(a\tau_{\rm H})^{1/3}\tau_a$, an approximation that is valid
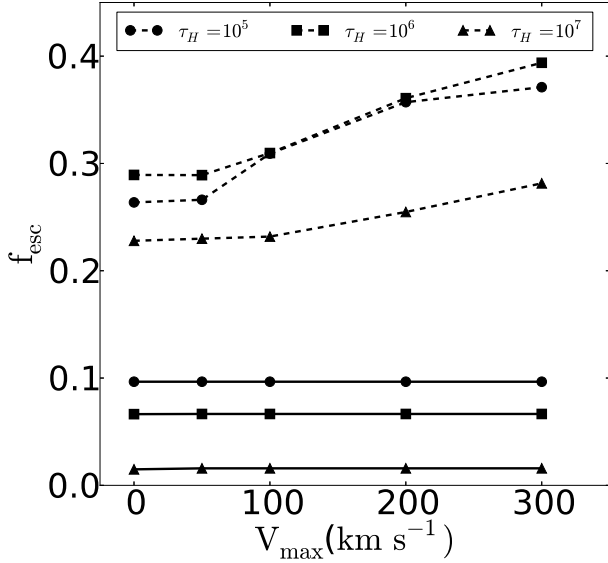
FIG. 6.— Escape fraction as a function of rotational velocity. All these models have $\tau_a = 1$. The continuous (dashed) lines correspond to central (homogeneous) models.
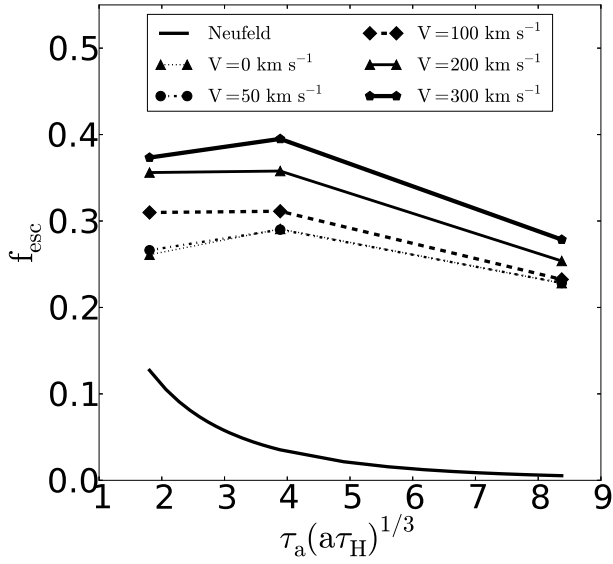

FIG. 7.— Escape fraction as a function of the product $(a\tau_{\mathrm{H}})^{1/3}\tau_a$. The analytic solution for the infinite slab is shown as a continuous line. Different dashed lines correspond to different rotational velocities. **IS THE ALBEDO TAKEN INTO ACCOUNT?**

only in the limit $a\tau_{\mathrm{H}} \gg 1$. The dashed lines in Figure 7 show the results for the different rotational velocities. First of all we note that the escape fraction does not increase from $\tau_{\mathrm{H}} = 10^5$ to $\tau_{\mathrm{H}} = 10^6$, a fact that is explained since there is a transition from a opaque to an extremely opaque medium which affect affects how Lyα photons escape from the medium: single flight vs. single excursion. **Que quiere decir eso de single flight y single excursion, porque explica eso la fraccion de escape?**

3.4. *Anisotropy and off-centered emission*

Rotation breaks the spherical symmetry of the static model and introduces the rotation axis as a preferred direction. This motivates us to study the anisotropy of the outgoing photons. In order to study possible devia-
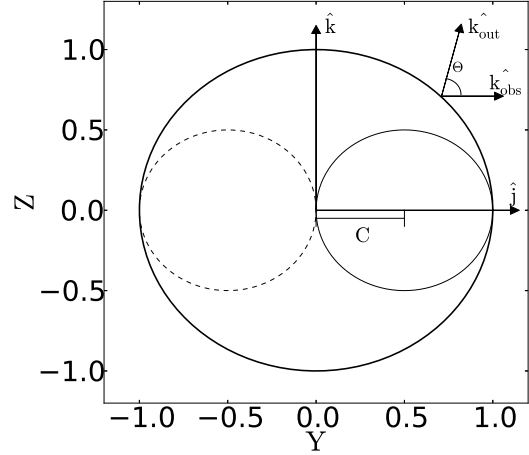

FIG. 8.— The two small circles show the two different spherical off-centered emitting regions with respect to the larger spherical gas distribution. The angular velocity vector is defined to be along the î direction (outwards the page). In order to study a possible anysotropy we place an observer along the the ĵ direction. The vector $\hat{k}_{\mathrm{out}}$ represents the outgoing direction of an escaping Lyα photon. **Si el observador esta en j, entonces las dos esferas no deberian estar sobre el eje k? Lo mejor es ademas hacer las dos circulos pequenos punteados.**
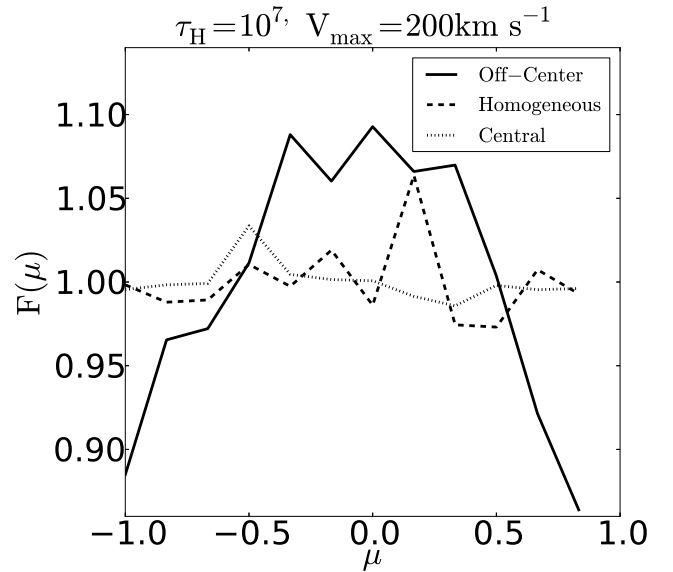

FIG. 9.— μ histogram showing the orientation effects for the different distributions central(Points line), homogeneous(Dashed) and off-Center(Solid line).

tions with respect to an isotropic flux we follow Zheng & Wallace (2013) to estimate the flux as a function of the angle Θ formed by the outgoing photons and the observer. Figure 8 presents a geometric scheme to clarify the definition of all relevant directions in the problem.

An estimator for the anysotropy is represented by

$$F(\mu) = \frac{2\Delta N}{N\Delta\mu}, \qquad (4)$$

where $\mu = \cos\Theta$, N is the total number of outgoing photons, ΔN is the number of photons in a angular bin $\Delta\Theta$. This definition satisfies the condition $\int_{-1}^{1} F(\mu)d\mu/2 = 1$. With this definitions, the isotropic emission is characterized by a flat $F(\mu)$ distribution.

Figure 8 presents the results for the $F(\mu)$ distribution for an sphere with $\tau_H = 10^7$ and $V_{max} = 200\,\mathrm{km\,s^{-1}}$. The dashed and dotted lines represent the homogeneous and central source distribution, respectively. This shows that the level of anisotropy induced by rotation does not surpasses the 5% level. We performed the same test with all the models and we do not fina any significant anisotropic effect.

We explore other kind of anisotropy by study the effect of radiation sources distributed with a different symmetry than the gas. To this end we select a subset of the photons in the homogeneous models such as they are emitted from off-centered spheres with respect to the gas distribution.

Figure 8 shows the two spherical regions we define to test for this effect. Each has a radius of $0.5R$, where R is the radius of the gaseus sphere. Provided that there is an observer located along the $\hat{j}$ direction, we pick two possible positions to center the spheres along the $\hat{k}$ axis: $\pm C\hat{k}$. In this configuration the emitting sphere centered on $+C\hat{k}$ moves away from the observer and the sphere centered on $-C\hat{j}$ moves towards the observer.

The variations in the μ distribution is shown in Figure 9, for the Off-Center model there is a strong dependence of the observed flux on the relative position of an observer with $\Delta\mu \leq 25\%$. In contrast,the central and homogeneous source distributions only show a weak anisotropy at the level of $\Delta\mu \leq 3\%$. The variations in μ does not depend on the rotational velocity while increasing the optical depth τ_H would also increase the variation of $\Delta\mu$ up to a 15%.

Figure 10 show the spectra for the two off-centered spheres located at $C = \pm 0.5R$. In this case we only use photons that have outgoing directions aligned with the observer i.e $|\mu| > 0.9$ & $|\mu| < 1.0]$. We do not find any asymmetry in the line produced by the off-center emission, the difference between the profiles corresponding to the spheres located at $C = -0.5R$ and that ones located at $C = 0.5R$ is negligible. As in the homogeneous/ central model the line gets broader as the rotational velocity increase also the central part of the line becomes predominant . There is also a signature of possible three peaks profiles for some models ($\tau = 10^6, V = 100, 200\,\mathrm{km\,s^{-1}}$and $\tau = 10^7, V = 200, 300\,\mathrm{km\,s^{-1}}$) which would be studied in detail in the next section.

3.5. *Three-Peak Profiles*

As mentioned above Off-centered emission shows signs of three peak profiles, to analyse this in more detail we use the same method of the spheres explained in §3.4. We select spheres at $C = (\pm 0.25R, \pm 0.5R, \pm 0.75R)$ with a radii of $0.25R$ for all the models, for those who present signs of three peak profiles such as ($V_{max} = 50 km\ s^{-1}$ & $\tau_H = 10^5$), ($V_{max} = 100 km\ s^{-1}$ & $\tau_H = 10^6$), ($V_{max} = 200 km\ s^{-1}$ & $\tau_H = 10^7$) we made another run with $\tau_\gamma = 10^6$ with the aim of get stronger profiles.

Figure 11 shows our findings, in order to get such profiles a relation between optical depth, rotational velocity and C must be accomplish. In particular we found that for the outer spheres $C = \pm 0.75$ the three peak arises for all of our models with $\tau_\gamma = 10^6$ this is due to the fact that the wings of the line move away from the central

part as C increase. Another requirement is that a high optical depth must be balanced with a high velocity in order to make the wings and the central peak similar in height, for models in which the velocity is low spheres at $C = \pm 0.25$ produce noise three peak profiles due to the high value of $\tau_{H,r}$.

Figure 12 show that even with a low resolution a three-peak profile would be observed, this is important for observational porpoises due to the finite spectral resolution.

4. DISCUSSION

Gas bulk rotation has a noticeable effect on the morphology of the Lyα line. In this section we discuss the implications of these findings for the interpretation of available observational data. Our discussion focuses on the qualitative aspects of diverse morphological features observed by Kulas et al. (2012) and Yamada et al. (2012)

We follow a classification of Lyα profiles made by Kulas et al. (2012). They presented observational results for star forming galaxies at $z = 2$-3 with multiple peaks in their Lyα emission. They classified the observed lines into five groups. In Group I the red peak is stronger than the blue, while in Group II the blue peak is stronger, in both cases the peaks are symmetrically located around the line center. In Group III the blue peak also dominates but there is an overall redward shift of the zero point. Group IV presents two similar peaks symmetrically located around the zero point and Group V galaxies show three peaks.

The asymmetries in Groups I, II and III cannot be explained by rotation. However, some galaxies in those groups have a high flux between the two peaks; an effect that can be induced by rotation. The same argument applies to galaxies in the group IV in which the flux in between of the two peaks is high ($\geq 70\%$ of the intensity in the highest peak). Finally, the triple peaked lines in Galaxies in Group V can be easily reproduced by rotation with off-centered emission given the right amount of asymmetry between the emitting region and neutral hydrogen distribution.

Another relevant sample of observations was presented by Yamada et al. (2012) for 91 LAEs at $z = 3.1$. They find that $\sim 33\%$ of the galaxies present a single peak profile. Some of the peaks have a strong symmetry, while others do not. The symmetric single peaked profile can be explained by rotation effects, while the asymmetric cases naturally arise in outflow/inflow models (Verhamme et al. 2008; Dijkstra et al. 2006). Among the 91 LAEs, 8 reveal triple peaked profiles with a central peak and two smaller peaks at the redder and bluer side, a feature that is present in our off-center emission models with rotation Figure 11.

The presence of single peaked profiles has been associated to inflow/outflow dynamics (**?**). In this paper we show that gas bulk rotation can also be considered as a probable origin for that behavior, provided that the observed single peak is highly symmetric. Similarly, in the case of double peaked lines with a high level of flux at the line center, rotation also deserves to be considered in the pool of possible bulk flows responsible for that feature, specially if the two peaks have similar intensities. The case of triple peaked lines is another clear feature of gas rotation under the additional condition of an off-centered emission.
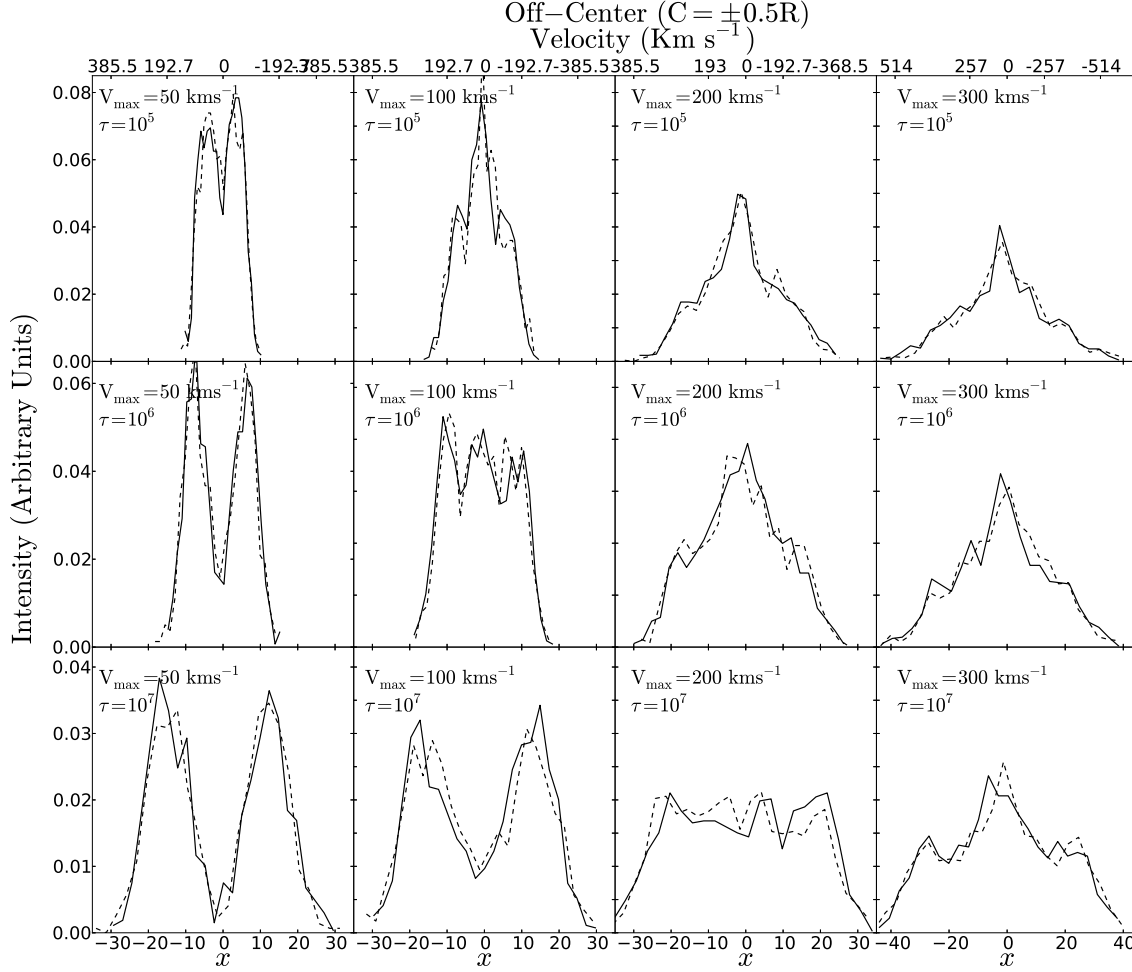
FIG. 10.— Lyα profiles for the off-center positions for all of our models, Dashed/solid lines represents spheres centered at $-0, 5R/ + 0.5R$ respectively.
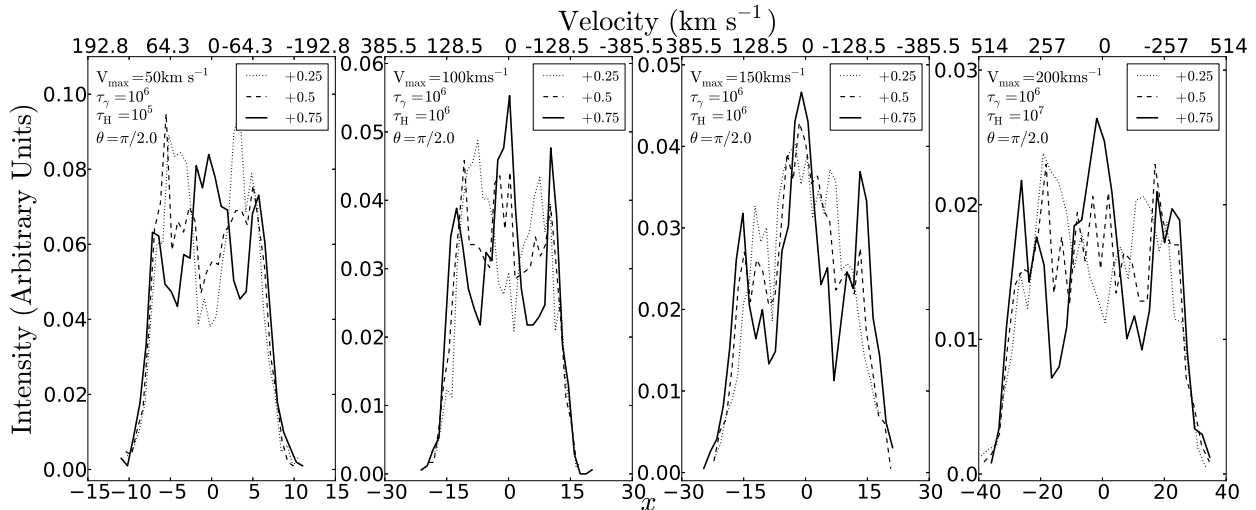

FIG. 11.— Three-Peak profiles for three different off-center positions $C = 0.25R$ (doted line), $C = 0.5R$ (dashed line) & $C = 0.75R$ (solid line) and for different rotational velocities.
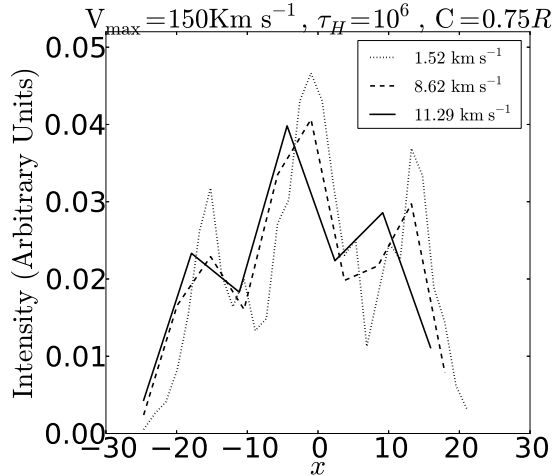
FIG. 12.— Three-Peak profiles for different resolutions:Low (Solid), medium(dashed), high(doted),

5. CONCLUSIONS

This paper quantifies for the first time in the literature the effects of rotation in the morphology of the Lyα emission line in star forming galaxies. The results are based on the study of an homogeneous sphere of gas with solid body rotation. We explore a range of models by varying the rotational speed, hydrogen optical depth, dust optical depth and initial distribution of Lyα photons with respect to the gas density. As a cross-validation, we obtain our results from two independently developed Monte-Carlo radiative transfer codes.

Our main result is that rotation clearly impacts the Lyα line morphology. Double peaked lines can make transitions into single peaked lines as the rotational velocity increases. In the case of off-centered emission result into triple peaked lines for certain values of optical depth and rotational velocities.

Quantitatively the main results of our study are summarized in the following items.

- The line width increases with rotational velocity. The line with approximately follows the functional form $W^2 = W_0^2 + (V_{max}/\lambda)^2$ where W_0 indicates the line width for the static case. λ is a constat determined from the radiative transfer results it is $\lambda_c = XX$ and $\lambda_h = YY$ for the central and homogeneous source distribution, respectively.

- A single peaked line emerges for high rotational velocities in the case of homgeneously distributed sources. The cases of single peaked lines occur when the rotational velocity is larger than the line width measured in the static case.

- For central sources we find that the number of scatterings does not significantly decrease with rotation, this is due to the fact that the vast majority of scatterings events are resonant, during which the mean free path is very short and the effect of gas bulk rotation is not enough to affect Lyα photons. The escape fraction does not depend on the rotational velocity neither the position of the peaks, but there is an increase in the flux on the central parts of the line for high rotational velocities.

- For homogeneous sources we find that the changes in the line morphology are linked to the reduction in the average number of scatterings. In the second part of §3.1 we show that, as rotational velocity increases, a large fraction of photons escape with less than 10 scatterings and on average with 40% less scatterings than in the static case. This makes highly improbable that a photon's frequency can move away from the line's center. In §3.1 For typical column densities of $N_{HI} = 1e^{19} - 1e^{20}$, we find that rotational velocities of 100-300 km s^{-1} broaden the line profile up to a factor of $2-3$ in comparison to the static case. Simultaneously, the flux in the line center also increases with rotational velocity. This increase induces the transition from a double peak to a single peak line in the models where the radiation sources are homogeneously distributed. Also the escape fraction increase by factors of $2-10$ with respect to the slab with centrally sources.

- For non-symmetric sources we find that three peak profiles could emerge for models in which the rotational velocity is the necessary to give rise to a central peak, but not that high to decrease the amount of photons in the wings. When initial off-center sources are selected from the outer parts of the galaxy the wings of the line are stronger. Also we do not find any considerable asymmetries in the line produced by off-center emission.

Comparing our results with recent observed LAEs we find that many morphological features such as high central line flux, single peak profiles and multi-peaked profiles could be explained by gas bulk rotation present in these LAEs.

REFERENCES

Adams, T. F. 1972, ApJ, 174, 439

Ahn, S.-H., Lee, H.-W., & Lee, H. M. 2000, Journal of Korean Astronomical Society, 33, 29

—. 2001, ApJ, 554, 604

Auer, L. H. 1968, ApJ, 153, 783

Avery, L. W., & House, L. L. 1968, ApJ, 152, 493

Barnes, L. A., Haehnelt, M. G., Tescari, E., & Viel, M. 2011, MNRAS, 416, 1723

Behrens, C., & Niemeyer, J. 2013, A&A, 556, A5

Dijkstra, M., Haiman, Z., & Spaans, M. 2006, ApJ, 649, 14

Dijkstra, M., & Kramer, R. 2012, MNRAS, 424, 1672

Forero-Romero, J. E., Yepes, G., Gottlöber, S., Knollmann, S. R., Cuesta, A. J., & Prada, F. 2011, MNRAS, 415, 3666

Forero-Romero, J. E., Yepes, G., Gottlöber, S., & Prada, F. 2012, MNRAS, 419, 952

Gawiser, E., Francke, H., Lai, K., Schawinski, K., Gronwall, C., Ciardullo, R., Quadri, R., Orsi, A., Barrientos, L. F., Blanc, G. A., Fazio, G., & Feldmeier, J. J. 2007, ApJ, 671, 278

Hansen, M., & Oh, S. P. 2006, MNRAS, 367, 979

Harrington, J. P. 1973, MNRAS, 162, 43

Koehler, R. S., Schuecker, P., & Gebhardt, K. 2007, A&A, 462, 7

Kulas, K. R., Shapley, A. E., Kollmeier, J. A., Zheng, Z., Steidel, C. C., & Hainline, K. N. 2012, ApJ, 745, 33

Laursen, P., Sommer-Larsen, J., & Andersen, A. C. 2009, ApJ, 704, 1640

Loeb, A., & Rybicki, G. B. 1999, ApJ, 524, 527

Neufeld, D. A. 1990, ApJ, 350, 216

Orsi, A., Lacey, C. G., & Baugh, C. M. 2012, MNRAS, 425, 87

Ouchi, M., Shimasaku, K., Akiyama, M., Simpson, C., Saito, T., Ueda, Y., Furusawa, H., Sekiguchi, K., Yamada, T., Kodama, T., Kashikawa, N., Okamura, S., Iye, M., Takata, T., Yoshida, M., & Yoshida, M. 2008, ApJS, 176, 301

Partridge, R. B., & Peebles, P. J. E. 1967, ApJ, 147, 868

Rhoads, J. E., Malhotra, S., Dey, A., Stern, D., Spinrad, H., & Jannuzi, B. T. 2000, ApJ, 545, L85

Schenker, M. A., Stark, D. P., Ellis, R. S., Robertson, B. E., Dunlop, J. S., McLure, R. J., Kneib, J.-P., & Richard, J. 2012, ApJ, 744, 179

Verhamme, A., Dubois, Y., Blaizot, J., Garel, T., Bacon, R., Devriendt, J., Guiderdoni, B., & Slyz, A. 2012, A&A, 546, A111

Verhamme, A., Schaerer, D., Atek, H., & Tapken, C. 2008, 111, 89

Verhamme, A., Schaerer, D., & Maselli, A. 2006, A&A, 460, 397

Yajima, H., Li, Y., Zhu, Q., Abel, T., Gronwall, C., & Ciardullo, R. 2012, ApJ, 754, 118

Yamada, T., Nakamura, Y., Matsuda, Y., Hayashino, T., Yamauchi, R., Morimoto, N., Kousai, K., & Umemura, M. 2012, AJ, 143, 79

Zheng, Z., & Miralda-Escudé, J. 2002, ApJ, 578, 33

Zheng, Z., & Wallace, J. 2013, ArXiv e-prints